



Numerical Modeling of the June 17, 2017 Landslide and Tsunami Events in Karrat Fjord, West Greenland

ALEXANDRE PARIS,^{1,3}  EMILE A. OKAL,² CYRIELLE GUÉRIN,³ PHILIPPE HEINRICH,³ FRANÇOIS SCHINDELÉ,³ and
HÉLÈNE HÉBERT³

Abstract—On June 17 2017, the western coast of Greenland was the site of a tsunami which flooded several villages, killing 4 people and destroying 11 houses in the village of Nuugaatsiaq. This tsunami was triggered by a subaerial landslide which occurred in a fjord 32 km ENE of Nuugaatsiaq. This paper presents the numerical modeling of this landslide of ~ 50 million m^3 and of the tsunami propagation from its source to Nuugaatsiaq. The landslide is considered as a granular flow under gravity forces and the water waves generated are related to the displacement of the sea bottom. The results obtained are similar in amplitude to our inferences from videos, *i.e.*, three water waves between 1 and 1.5 m arriving at Nuugaatsiaq with a period of roughly 3 min, and are also in general agreement with the amplitude (1 m) resulting from deconvolution of oscillations recorded on a horizontal seismogram operating at Nuugaatsiaq (NUUG). According to the field survey performed by Fritz et al. (EGU General Assembly Conference Abstracts, Vol. 20 of EGU General Assembly Conference Abstracts, p 18345, 2018a) on July 2017, a second mass next to the landslide is threatening Karrat Fjord. A sensitivity study is realized on its volume, with 2, 7, 14 and 38 million m^3 reaching the sea. The shape of the water waves is found to be independent of volume, and linearity is observed between the volume and the water wave heights. Finally, the orientation of the slide does not seem to influence either the period or the shape of the generated water waves.

Key words: Tsunami, landslide, Greenland, simulation.

1. Introduction

Tsunamis generated by landslides, either subaerial or submarine, can be as dangerous for coastal populations as earthquake-generated tsunamis (Thomson

et al. 2001; Synolakis et al. 2002). Because landslides are often (but not always) triggered by major earthquakes, and because, especially in the marine environment, they can remain conspicuously hidden to direct observation, it can occasionally be difficult to determine the exact generation process of major tsunamis (Geist 2000; Okal and Synolakis 2001; Synolakis et al. 2002). On the other hand, the different physical nature of the source has allowed the definition of robust discriminants (Okal and Synolakis 2003). A review of problems associated with a simulation of landslide tsunamis can be found for example in Fine et al. (2003).

Subaerial landslides, which initiate above sea level and penetrate the water column, pose additional challenges. Their aerial components lend themselves to direct observation, which can provide important constraints on the initial dynamics of the sliding process. However, their evolution into the water column, and in particular the degree of cohesion of the material, is often poorly documented. The landmark subaerial slide remains to this day the Lituya Bay event of 10 July 1958, which was triggered by a major strike-slip earthquake on the Fairweather fault in the panhandle of Alaska (Miller 1960) and resulted in a record-breaking 525-m run-up on the opposite side of Gilbert Inlet, a geometry repeated on a smaller scale during the 2007 Aysén earthquake in Southern Chile (Sepúlveda and Serey 2009). By contrast, “orphan” subaerial landslides have taken place in the absence of any detectable seismic trigger, a typical example being the 1999 event at Fatu Hiva, Marquesas (Okal et al. 2002; Hébert et al. 2002). The 2015 Taan Fjord landslide at Icy Bay, Alaska featured a geometry of sliding strikingly similar to that of the 1958 Lituya

¹ Laboratoire de Géologie, Ecole Normale Supérieure, CNRS UMR8538, PSL Research University, Paris, France. E-mail: alexandre.antoine.paris@gmail.com

² Department of Earth and Planetary Sciences, Northwestern University, Evanston, IL, USA.

³ CEA, DAM, DIF, 91297 Arpajon Cedex, France.

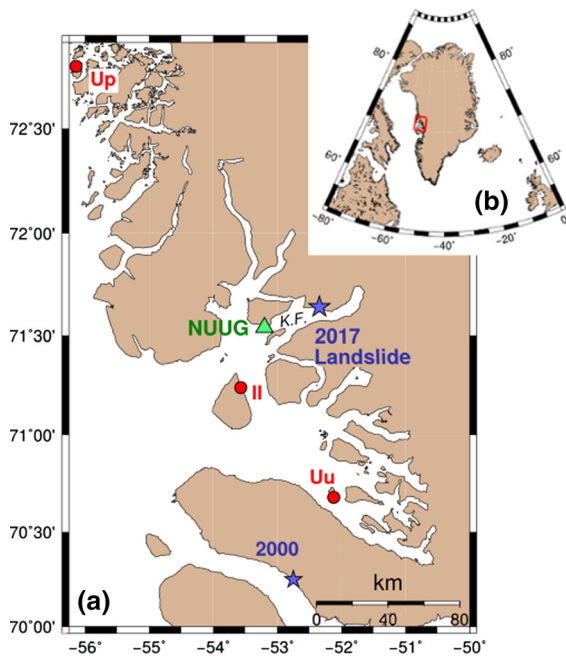


Figure 1

a Close-up Mercator projection of the western coast of Greenland, showing location of the 2017 landslide (star) in Karrat Fjord (K.F.), and of the village of Nuugaatsiaq (triangle). The red dots identify other locations where the tsunami was observed (II Illorsuit, Up Upernavik, Uu Uummannaq). The location of the 2000 slide is also shown. **b** Map of Greenland showing boundaries of the close-up map (a) in thick red

Bay event, albeit on a smaller scale reaching “only” 193 m of run-up, and with no detectable seismic trigger (Higman et al. 2018). Subaerial landslides have been studied in the laboratory and successfully modeled analytically, notably by Fritz (2002), Weiss et al. (2009) and Viroulet et al. (2013).

This paper deals with a subaerial landslide that occurred on June 17, 2017, on the Northern slope of the Karrat Fjord along the western coast of Greenland (see Fig. 1 for context and location). It was followed by a tsunami which was observed in several villages up to a distance of 160 km. In Nuugaatsiaq (pop. ~ 80), 11 houses were damaged or washed away, 4 persons were reported killed or missing, and 9 injured (Clinton et al. 2017). Several videos,¹ posted on the

Internet after the event, document water flooding houses in Nuugaatsiaq. Thanks to the ruler tool and the location of houses at different times before and after the event on GoogleEarth, the maximum inundation length is estimated at 150 m and maximum run-up heights at about 10 m in Nuugaatsiaq.

The 2017 landslide was identified the next day by an aerial survey of the Arktisk Kommando of the Danish Defence,² about 32 km ENE of Nuugaatsiaq, upstream Karrat Fjord. The failed mass consists of a portion of bluff about 1000 m wide and 500 m tall (see red ellipse on Fig. 2); its scar is well identified on photographs from the aerial survey, and from before-and-after satellite imagery. We note (see blue ellipse on Fig. 2) that a second mass seems about to fail, immediately to the West of the 2017 slide.

As discussed below, three previous landslide-generated tsunamis had been documented in Greenland in 1954, 2000 and 2012, with the 2000 event similar in nature to the 2017 one, making this kind of event a recurring hazard in the region.

The 2017 landslide in Karrat Fjord was detected as a seismic event worldwide (up to distances of 95°); however, the NEIC of the USGS did not locate the event, but simply used the location reported from satellite imagery (71.640°N; 52.344°W), for which they obtained an origin time of 23:39:12 GMT. The event was given magnitudes $M_L = 3.3$, $m_b = 3.6$ and $M_s = 4.0$ by the International Data Center of the CTBTO, and $M_s = 4.2$ by the NEIC. The growth of magnitude with period is typical of a non dislocative event, whose source is expected to have a longer duration than a genuine seismic source of comparable size, and as a result to be deficient in high frequencies (Okal 2003).

In addition to teleseismic recordings, the 2017 Karrat Fjord event was observed in Nuugaatsiaq (NUUG) on a 3-component Streckeisen STS-2 seismometer operated by the Danish Geological Survey. As will be detailed in Sect. 3.3, a remarkable aspect of the resulting waveforms is that they include a quantifiable recording of the tsunami, a priceless occurrence in the absence of a tidal gauge station.

¹ To see the videos, click on the links below:

<https://www.youtube.com/watch?v=jBmkT5y52ng>
<https://www.youtube.com/watch?v=LzSUDbSsPI>
<https://www.youtube.com/watch?v=amWshLXe74s>
<https://www.youtube.com/watch?v=tWvYFMo2LsQ>.

² Photos of the aerial survey are visible here: <https://goo.gl/XRJomU>.



Figure 2

Aerial photograph of the 2017 slide (red ellipse) and the western potential landslide (blue ellipse)

The purpose of this paper is to provide a numerical modeling of the landslide and of the tsunami, as well as a quantitative interpretation of the seismic record at NUUG. We model both the Karrat slide and its tsunami using the numerical code *Avalanche* (Heinrich et al. 2001a), developed at the Commissariat à l'énergie atomique et aux énergies alternatives, and widely applied in previous landslide studies, both submarine (Rodriguez et al. 2013; Poupardin et al. 2017) and subaerial (Heinrich et al. 2001b). Assuming the collapse of a 53 million m³ landslide, we simulate water waves of 1–1.5 m amplitude, at 8 m water depth, reaching the village after 8 min.

In addition, we simulate the potential failure of the “second”, precarious mass identified to the West of the 2017 slide (see blue ellipse on Fig. 2), using several volume scenarios, the purpose being to try to identify the potential threat for the village of Nuugaatsiaq.

2. Previous Similar Events

Three other tsunamis are documented for Greenland in the NOAA/PMEL database in 1954, 2000 and 2012. However, the 1954 event is a rogue wave

whose origin is undetermined (ICAO 1955), and that in 2012 is due to calving of a fjord glacier into the ocean (NOAA 2018). By contrast, the November 21, 2000 tsunami, investigated in detail by Pedersen et al. (2002) and Dahl-Jensen et al. (2004), is directly comparable to the 2017 event. It consisted of a large volume of 90 million m³ of rock, sliding at Paatut, only 155 km South of Karrat Fjord, between altitudes of 1400 and 1000 m, of which 30 million m³ sunk into the ocean. The resulting tsunami reached a height of 50 m at the source, and inundated 250 m for a run-up of 28 m at the village of Qullissat which, fortunately, had been abandoned 28 years earlier. Dahl-Jensen et al. (2004) also document another tsunami-genic landslide at Qullissat in 1952, which killed 1 person.

Landslides having generated tsunamis of comparable characteristics have been described worldwide and can be triggered by several mechanisms. Paramount among them are local earthquakes, in a context reminiscent of the record 1958 event at Lituya Bay (Miller 1960): for example, the 2007 landslides in Aysen, Southern Chile (Naranjo et al. 2009), totalling ~ 20 million m³ in volume, generated a tsunami which ran up ~ 30 m at the source and 14 m on the

opposite side of the fjord, following a strike-slip earthquake of magnitude $m_b = 6.1$, only 30 km away. Volcanic eruptions can result in the build-up of unstable or precarious structures, failing through large scale submarine or aerial landslides, as happened on December 30, 2002, at Stromboli, Italy, with two slides separated by 7 min, one submarine (20 million m^3), the other aerial with a volume of 4–9 million m^3 (Tinti et al. 2006). The aerial one was more similar to the 2017 Karrat case, as it had an altitude of 550 m, and generated waves 12 m high at a village located 2 km away.

In many cases, the triggering mechanism is of such small magnitude as to remain unnoticed. That would be the case, for example, of the 1999 Fatu Hiva landslide in the Marquesas Islands (4 million m^3 of brecciated volcanic material), which flooded the nearby village of Omoa (Hébert et al. 2002; Okal et al. 2002), or of the large, tragic landslides in Norwegian fjords described by Hermanns et al. (2006) at Taffjord (1934) and Loen (1905 and 1936), the latter involving the closed Lovatnet lake. The Taffjord failure (1.5 million m^3) took place ~ 800 m above sea level and produced a tsunami which ran up 62 m and killed 41 people; the 1905 Loen failure was smaller (0.4 million m^3) but its tsunami ran up 41 m, and killed 61 people, while the 1936 slide involved 1 million m^3 , a 74-m runup and 73 fatalities. The 2007 landslide into Chehalis Lake, B.C. involved 3 million m^3 of rock and produced a run-up of 38 m on the opposite side of the lake (Wang et al. 2015), fortunately without loss of life. A particularly tragic case of a landslide-generated tsunami in a closed lake occurred in 1963 in the Vajont reservoir in Northern Italy, where a 200-m tall splash overtopped the dam and wiped out the village of Longarone in its lee, killing upwards of 1900 people (Ward and Day 2011). A possible, if not probable, repeat of this situation at Sarez Lake, Tajikistan could reach even more catastrophic dimensions, as it would probably destroy the precarious natural dam holding the lake, itself the result of the blockage of the valley by a much larger, 2.4-km³ landslide during the earthquake of 18 February 1911 (Schuster and Alford 2004; Ambraseys and Bilham 2012).

With the exception of the latter, the selection of events listed above are generally comparable to the

2017 Karrat Fjord landslide. In the context of global warming, and of the melting of ice caps, it is expected that the weakening of permafrost will lead to an increase in catastrophic landslides in that part of the world (Haeberli and Gruber 2009; Huggel et al. 2012).

3. Observations of the 17 June 2017 Event

3.1. Numerical Reconstruction of the Landslide

In order to perform a numerical modeling of the landslide, two digital surface models (DSM) of the area were compiled before and after the event. The “before” DSM was realized from Spot6 stereoscopic images, acquired on July 22, 2013 at 1.5-m spatial resolution. The “after” DSM was obtained from Pleiades tri-stereoscopic images, acquired right after the event, on July 08, 2017, at 0.7-m spatial resolution, with estimated 1 m in vertical precision (Guérin et al. 2014).

The DSMs are calculated through an automatic pipeline which performs the data co-registration and the DSM generation, as described in Guérin et al. (2014). The data co-registration is realized as a preprocessing step in order to ensure that the image (and hence the DSM) are finely registered between them. This operation consists in a bundle-block adjustment of all the available data which can be performed without any Ground Control Points (GCP), as none are available over the area of interest. The complete methodology is presented in Guérin (2017) and is based on a tie-points detection according to a pairwise image correlation followed by an iterative refinement of the image acquisition models provided as Rational Polynomial Coefficients. Tie-points detection remains a sensitive part of the method, especially when dealing with areas featuring steep slopes. In order to get accurate tie-points, the detection is then performed on the images after their orthorectification with the most accurate digital terrain model (DTM) available (Guérin 2017).

Once the registration is performed, the DSMs are generated at each date according to the methodology described in Guérin et al. (2014) and based on so-called ground space image matching, performed with

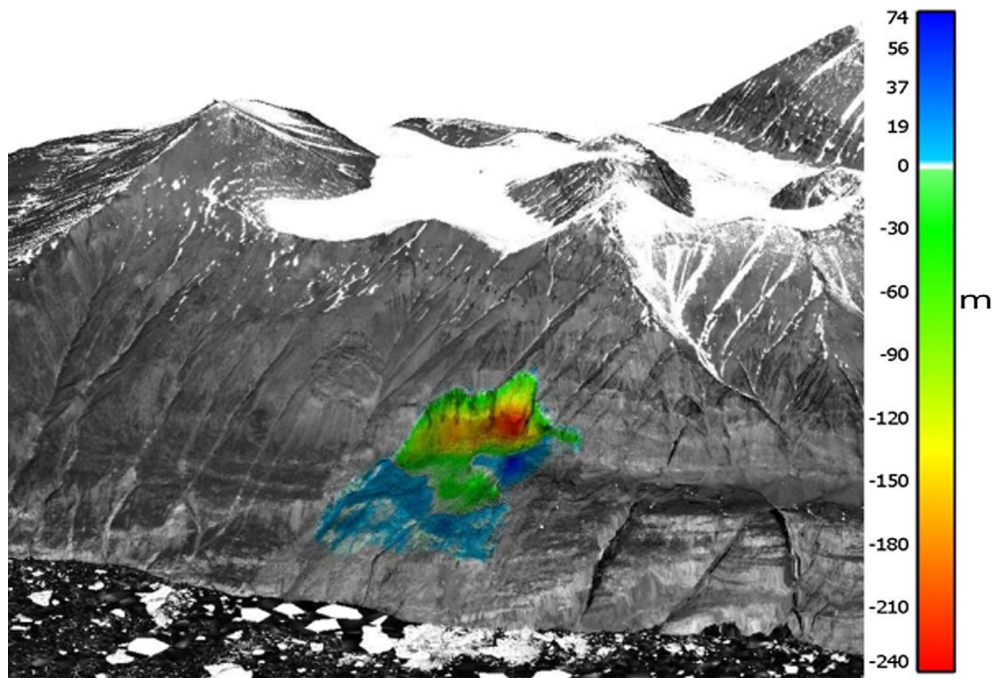


Figure 3

Difference between the “before” and “after” digital surface models (DSM), superimposed on the “after” DSM, computed from the pleiades tri-stereoscopic images from 2017. The variations of the difference elevation values (in m) are represented with the color bar

the open source software MICMAC, developed by the French National Geographic Institute (IGN) (Pierrot-Deseilligny and Paparoditis 2006). This methodology allows the calculation of an elevation value for each point on a grid defined on the ground space with both planimetric and altimetric steps. In practice, for each ground point of the grid, the image coordinates are obtained according to refined acquisition models of the images that link the ground position of the point and its coordinates on the images. A correlation score is then computed between pixel windows selected over each image and at each altitude of the grid. The final altitude value is chosen considering the correlation score and a regularization term (Guérin et al. 2014). Figure 4 represents the DSM obtained from the pleiades tri-stereoscopic images acquired after the event. For this study, both DSM were generated with a 2 m planimetric step and 1 m altimetric step.

Finally, one computes the difference between the DSMs, at the same resolution and hence perfectly comparable. Figure 3 represents the resulting differential DSM over the collapsed area, superimposed on

the “after event” DSM. We use it to infer that the collapsed area reached a height of 240 m and a total volume of 48 million m^3 . However, part of this volume did not spill into the ocean, as confirmed by the presence of important subaerial debris on the mountain side (Fig. 2); we estimate a volume of 45 million m^3 for the effective spill into the ocean. The inferred width of the slide is 1000 m, and its length 500 m (Fig. 4).

These numbers are in general agreement with Gauthier et al. (2018), who describe the Karrat landslide as a rock avalanche of 58 million m^3 , of which only 45 million m^3 reached the water, the slide being initially 950 m wide and 800 m long, at altitudes between 800 and 1200 m. The origin of the 10% discrepancy in volume may be rooted in the decimation of the high-resolution satellite images (sampled at 1.5 and 0.7 m) when building the simulation grid (sampled at 25 m).

In a recent contribution, Chao et al. (2018) have used regional recordings of the Karrat Fjord event across Greenland to invert the source characteristics, using Ekström and Stark’s (2013) methodology. They

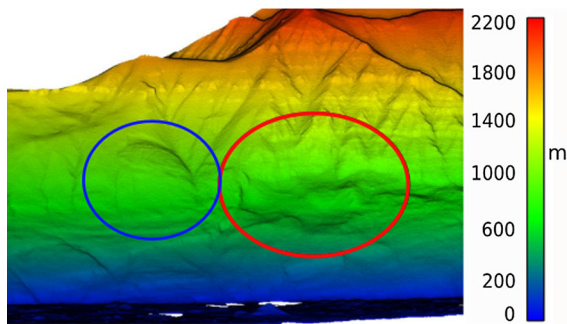


Figure 4

Digital surface model computed from the Pleiades tri-stereoscopic images from 2017 with a 2 m planimetric step and a 1 m altimetric step. The color bar corresponds to the elevation values (in m). The red ellipse identifies the collapsed area; the blue ellipse identifies the potential West slide

obtain a significantly larger volume penetrating the sea of about 75 million m³.

3.2. Damage

The tsunami reached and flooded the two main villages in the area, first Nuugaatsiaq, 32 km WSW of the landslide, and later Illorsuit, an additional 35 km to the SSW. At Nuugaatsiaq, 4 people were killed and 11 houses were completely washed away by the water waves. Figure 5 shows examples of damage by the tsunami at Nuugaatsiaq. Much smaller impact and flood were observed at Illorsuit.

GoogleEarth images taken before and after the event clearly show holes where houses once stood (Fig. 6), which document scouring of their foundations, possibly during an ebbing phase. Several photos and videos taken during the event are available and allow a further evaluation of the damage caused by the tsunami. On some videos,³ recording starts before any visually detectable wave arrival, which suggests a first wave with either a negative amplitude (leading depression, withdrawal), or a positive one of very small amplitude.

One of the videos⁴ shows the water waves stopping before the cemetery at Nuugaatsiaq. As an effect of perspective, the exact line of inundation is

difficult to evaluate. According to GoogleEarth, the distance between the coast and the cemetery is about 200 m, so we can conclude that the inundation distance was about 150 m at this location, with an estimated run-up of about 10 m.

3.3. Analysis of the Seismic Signal

Figure 7 shows a record of the event at the seismic station NUUG (71.538°N, 53.200°W), located at Nuugaatsiaq, 32 km from the landslide, and part of the Danish Seismological Network. Note that the horizontal components were, at the time, rotated 79° clockwise from their standard orientation (Clinton, pers. comm., 2018). In addition to classical *P* and *S* phases (interpreted here as crustal *P_g* and *S_g*), a long-period oscillation with a period of about 3 min is present starting at 23:47 GMT, *i.e.*, 8 min after the body waves. This waveform is much too late to be interpreted as a traditional surface wave from the same source as the body waves (as it would have reached NUUG in at most 15 s); we also note that it is not observed at others stations in Greenland and across Baffin Bay in Canada. Accordingly, we tentatively interpret it as a seismic record of the tsunami.

We note the remarkable similarity between the waveforms obtained at NUUG and those recorded at Panarea Island during the tsunamigenic landslides of 30 December 2002 at Stromboli Volcano, Italy (La Rocca et al. 2004). In particular, a spectrogram analysis of the S11°E seismogram (Fig. 8) shows that the long-period oscillation is peaked between 6 and 8 mHz, within the range of frequencies (6–15 mHz) quoted by La Rocca et al. (2004).

However, we observe on Figs. 7 and 9 that the principal component of ground motion is horizontal and polarized in the direction N20°W which is close to 90° away from the azimuth from NUUG to the source ($\beta = 69^\circ$), as was the case at Panarea. Rather, the observed polarization of the signals at NUUG is essentially across the width of the narrow Karrat channel offshore of Nuugaatsiaq (Fig. 9), and as such reminiscent of the geometry of seiche reported in the Panama Canal by McNamara et al. (2011), where the seismic signals recorded by a local seismometer were polarized perpendicular to the axis of the canal. This observation indicates that part of the wave

³ This video for example:
<https://www.youtube.com/watch?v=amWshLXe74s>.

⁴ Around 0:46 on this video:
<https://www.youtube.com/watch?v=jBmkT5y52ng>.



Figure 5

a, b Examples of damage from 2017 at Nuugaatsiaq. **c** Screenshot from a YouTube video (<https://www.youtube.com/watch?v=jBmkT5y52ng>) showing the tsunami flooding Nuugaatsiaq. The blue house is being washed away. Rocks in the foreground delimit the cemetery of Nuugaatsiaq. The running man (yellow arrow) escaped safely

activity in the channel, as recorded on the NUUG seismometer, may involve seicheing of the channel.

In the absence of a tidal gauge at Nuugaatsiaq, we next attempt to quantify the seismic record in order to obtain an estimate of the amplitude of the tsunami in Karrat Fjord. For this purpose, we recall that seismic recording of tsunamis was documented in the far field by Yuan et al. (2005) and Hanson and Bowman (2005) at stations located on islands in the Indian Ocean during the 2004 Sumatra tsunami. Using Ward's (1980) representation of tsunamis as a special branch of the Earth's normal modes, Okal (2007) later showed that such recordings could be successfully interpreted and quantified by assuming that the horizontal seismometer is simply deployed on the ocean floor in the absence of the island, and responds to the combination u_x^{app} of the horizontal displacement of the solid Earth, of the tilt induced on the ocean floor by the passage of the tsunami wave, and

of a change of gravitational potential accompanying the tsunami, as detailed by Gilbert (1980), who had been motivated by the need to apply small corrections (of at most 10%) to the precise quantification of the conventional spheroidal modes of the Earth. By contrast, Okal (2007) showed that these "corrections" could reach several orders of magnitudes in the case of tsunami modes, and defined a "Gilbert Response Function", $GRF(\omega)$, that could be used in the frequency domain to restore the spectral amplitude of the vertical sea-surface motion of the tsunami, $\eta(\omega)$, from that of the apparent ground motion recorded by the instrument, $u_x^{app}(\omega)$:

$$\eta(\omega) = \frac{u_x^{app}(\omega)}{GRF(\omega)} \quad (1)$$

with $GRF(\omega)$ readily computed from the various components of the tsunami eigenfunction at the ocean floor:

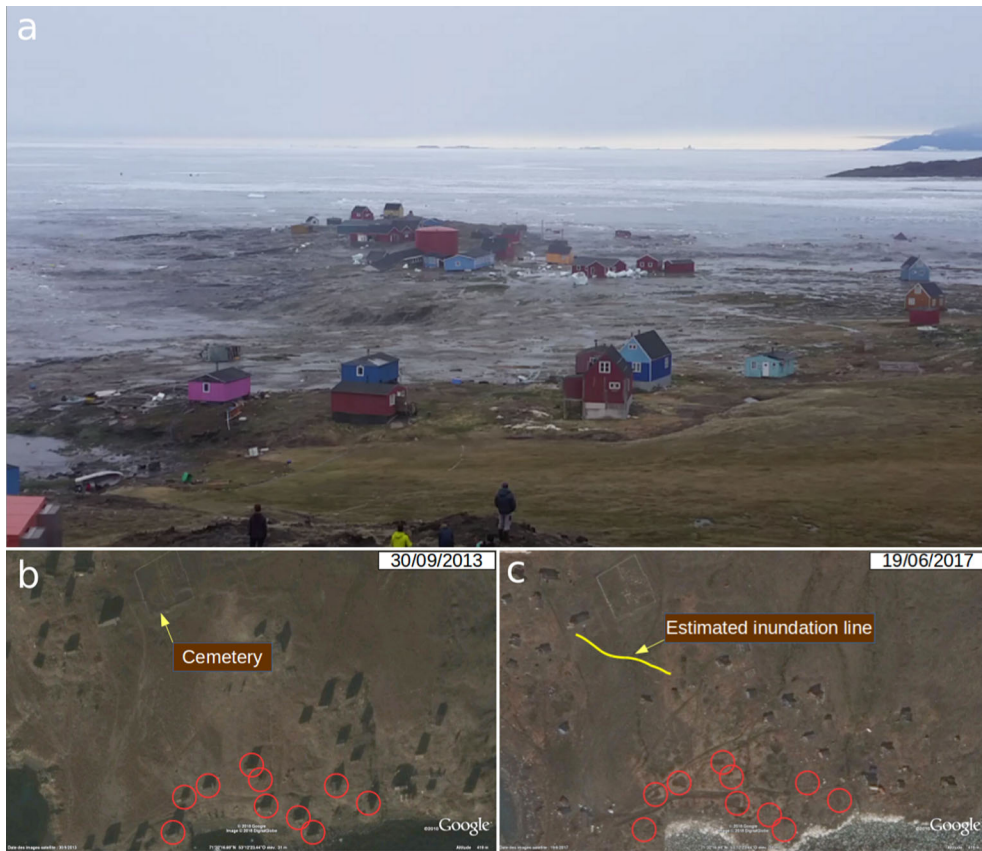


Figure 6

a Looking south, view of Nuugaatsiaq in the aftermath of the tsunami, identifying the inundated zone. Photo from: <https://goo.gl/2CYybt>. **b**, **c** GoogleEarth images before (30/09/2013) and after (19/06/2017) the event. The yellow line represents the estimated inundation line of the tsunami. Red circles surround the houses washed away by the water waves

$$GRF(\omega) = ly_3 - \frac{l}{r\omega^2}(gy_1 - y_5) \quad (2)$$

in the notation of Saito (1967) and with all details given in Okal (2007).

Despite the extreme simplifying assumptions of this model (ignoring the island or receiving shore), Okal (2007) showed in particular that a deconvolution of a seismic recording using (1) compared favorably with time series obtained on the high seas by DART buoys, and could actually be used quantitatively to estimate an acceptable value of the seismic moment of the parent earthquake.

In the present case, and notwithstanding the added complexity of the probable seiche in Karrat Channel, we adapt the formalism to the case of propagation in very shallow waters, ranging from a probable 400 m in the fjord to ~ 100 m in the

channel facing the village of Nuugaatsiaq. In this context, a remarkable aspect of the function $GRF(\omega)$ is that it is essentially independent of water depth H . This property had been verified numerically in the range $H = 4\text{--}5$ km and a simple justification provided, in the Appendix to Okal (2007). On Fig. 10 we extend this investigation by computing systematically values of $GRF(\omega)$ for ocean models with depths varying between 100 m and 4 km; we verify that this function varies only minimally with H , and can be approximated by regressing it logarithmically as

$$\log_{10} GRF(\omega) = -2 \log_{10} f - 1.317 \quad (3)$$

where f is the frequency in mHz and the slope has been forced to the exact value -2 , on the basis of the approximation suggested in Equation (A.3) of Okal (2007); we further verify that the constant (-1.317)

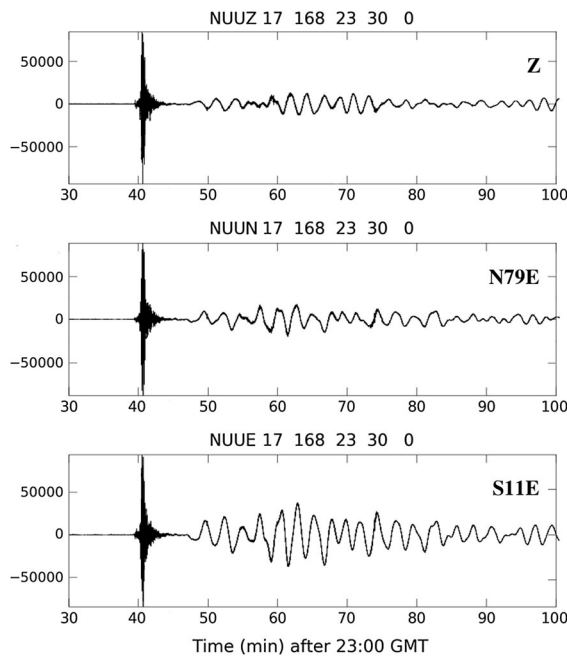


Figure 7

Three-component record of the 2017 Karrat landslide and tsunami at Nuugaatsiaq (NUUG), 32 km away. These are raw seismograms, expressed in digital units, and uncorrected for instrument response (common to the three components). Note that the horizontal components were misoriented, and therefore recorded motion along the N79°E and S11°E directions, respectively (Clinton, pers. comm., 2018). The tsunami is recorded as the long-period oscillation starting at 23:47 GMT; note that it is maximum on the S11°E component

is in excellent agreement with the value predicted by that equation, assuming a rigidity $\mu = 4 \times 10^{11}$ dyn/cm², intermediate between crustal and mantle values.

Equation (3) expresses the response to a tsunami of the ocean-solid Earth system in terms of an apparent horizontal displacement of the ocean floor. It is then possible to combine it with the instrument, in our case the STS-2 operated at NUUG. The latter has a broadband *velocity* response, essentially flat below 100 s, before falling like ω^2 at longer periods. This means that the resulting combination has a *displacement* response peaked around 100 s (10 mHz), and falling like ω and ω^{-1} , respectively on each side; in other words, an STS-2 recording a tsunami acts like a moderate band-pass filter centered around 10 mHz.

In this context, we present on Fig. 11 the result of the deconvolution of the S11°E component of the NUUG record of the Karrat Fjord event. This figure is

conceptually similar to Figure 10 of Okal (2007), except for adjusted bandwidth parameters. Frame (a) reproduces the raw seismogram in Fig. 7. Frame (b) shows the result of deconvolving the instrument response in the frequency band 1.7–17 mHz, and thus represents the apparent horizontal motion of the ocean floor, $u_x^{app.}(t)$; note that this particular time series has no direct mechanical interpretation. Finally, Frame (c) is obtained by deconvolving the Gilbert Response Function and is thus representative of the particle motion $\eta(t)$ at the surface of the ocean. We recall that Okal (2007) was able to compare favorably the amplitude of the similarly deconvolved record of the 2004 Sumatra tsunami at Amsterdam Island with that of the direct detection of the tsunami by the JASON altimeter satellite (Scharroo et al. 2005), therefore validating the deconvolution procedure. In the present situation, a major unknown regarding the propagation of the tsunami remains the poorly charted and *a priori* variable depth H of the water column, but as we have seen, the function $GRF(\omega)$ is independent of H , which further justifies our procedure. Finally, we have verified that the spectrogram of the resulting time series $\eta(t)$ does not differ significantly from Fig. 8, with maximum spectral amplitudes in the 6–8 mHz range.

We conclude that the record of the tsunami by seismic station NUUG suggests an offshore zero-to-peak amplitude of ~ 1.9 m. However, we note that this maximum is reached only 15 min after the first arrival (around 00:02 GMT on the 18th), probably under the influence of seiche. During the first 10 min, corresponding to the time window of our simulations, the maximum wave amplitude is only ~ 1 m.

4. Methods

4.1. Landslide Model

For the purpose of simulating the tsunami generated by the Karrat landslide, we use the parameters determined in Sect. 3.1 as a source condition. Some authors (Løvholt et al. 2008; Abadie et al. 2012) generally use a 3D model for such landslides, with full 3D Navier-Stokes equations applied to

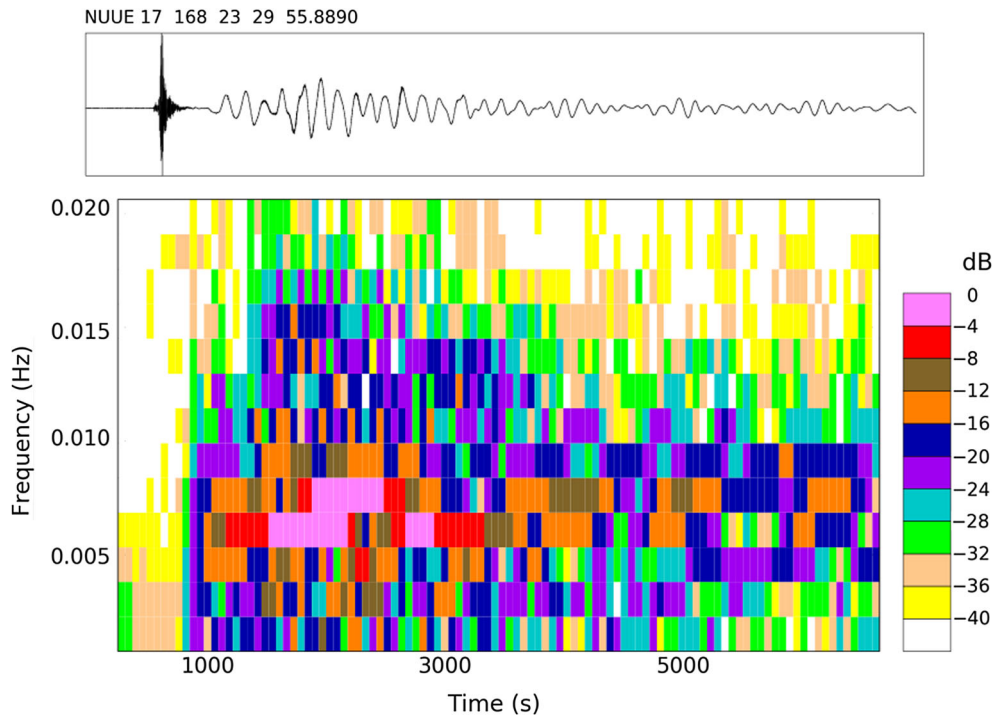


Figure 8

Spectrogram of the raw S11°E seismogram at NUUG. A standard Fourier transform is performed in a 600-s long window moving across the seismogram in increments of 60 s, and the resulting spectral amplitude in each time and frequency pixel is color coded according to the logarithmic scale at right. Note the dominant frequency component between 6 and 8 mHz

multimaterial flow. Here, and following our previous studies, we use a simpler, depth-averaged model to simulate both the landslide and the propagation of water waves (Assier-Rzadkiewicz et al. 2000; Labbé et al. 2012).

Examination of photos of the scar suggests that the landslide can be considered as a homogeneous, incompressible fluid-like flow of granular material following a Coulomb-type friction law. We further assume that the entire mass suddenly fails in one block after losing its equilibrium, and that it has no initial velocity.

For simplicity, basal friction is modeled in this study by a Coulomb-type friction law with a constant friction angle. This hypothesis may show limitations, since the friction angle depends on the velocity, as shown by laboratory experiments on granular flows but it should also be valid in the case of a rough bed with high inclination angles (Pouliquen 1999).

Following the one-phase grain-flow model of Savage and Hutter (1989) and taking into account

Coulomb basal friction and gravity, we model the slide by solving the equations of conservation of mass and momentum in a (x', y') coordinate system linked to the topography :

$$\frac{\partial h_s}{\partial t} + \frac{\partial}{\partial x'}(h_s u_s) + \frac{\partial}{\partial x'}(h_s v_s) = 0; \quad (4)$$

$$\begin{aligned} & \frac{\partial}{\partial t}(h_s u_s) + \frac{\partial}{\partial x'}(h_s u_s^2) + \frac{\partial}{\partial y'}(h_s u_s v_s) \\ &= -\frac{1}{2} \kappa \frac{\partial}{\partial x'}(g h_s^2 \cos \theta) + \kappa g h_s \sin \theta_{x'} + F_{x'}; \end{aligned} \quad (5)$$

$$\begin{aligned} & \frac{\partial}{\partial t}(h_s v_s) + \frac{\partial}{\partial x'}(h_s v_s u_s) + \frac{\partial}{\partial y'}(h_s v_s^2) \\ &= -\frac{1}{2} \kappa \frac{\partial}{\partial y'}(g h_s^2 \cos \theta) + \kappa g h_s \sin \theta_{y'} + F_{y'} \end{aligned} \quad (6)$$

where h_s is the slide's thickness in a direction perpendicular to the slope, $\mathbf{u} = (u_s, v_s)$ the depth-averaged velocity vector parallel to the bed, $\kappa = 1 - \rho_w/\rho_s$ where ρ_w and ρ_s are the water and rock densities with a ratio $\rho_s/\rho_w = 1.7$ (for the subaerial part of the slide, κ is identically equal to 1), $\theta(x, y)$

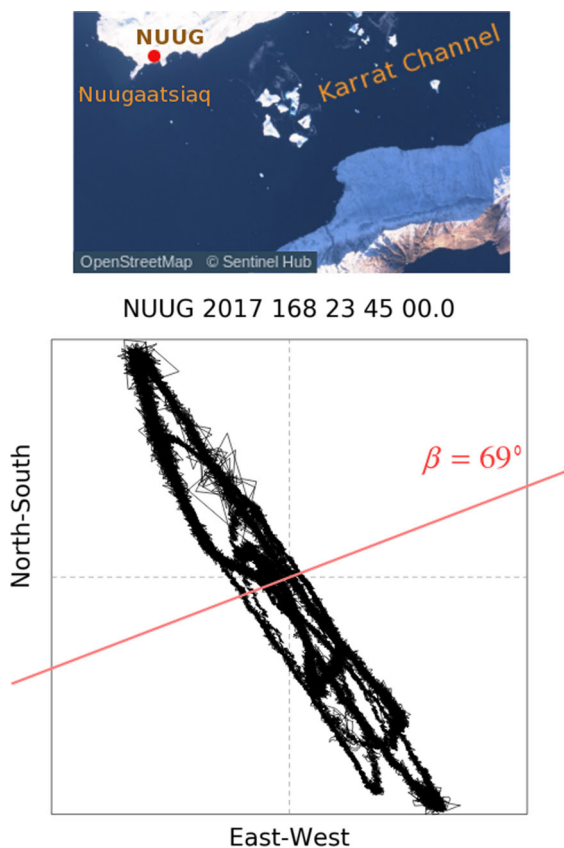


Figure 9

Two-dimensional plot of the horizontal components of the seismogram at NUUG, after counterclockwise rotation of 79° to correct for instrument misorientation (Clinton, pers. comm., 2018). The time window starts at 23:45 GMT and lasts 55 min, thus excluding the seismic waves. Note that the motion is not polarized in the direction of the back-azimuth to the epicenter ($\beta = 69^\circ$), shown as the red line, but rather across the Karrat Channel (Sentinel inset at upper), whose width is ~ 3.5 km in front of Nuugaatsiaq. On the scale of the inset, the red dot corresponds to the location of station NUUG

the local steepest slope angle, $\theta_{x'}$ and $\theta_{y'}$ the slope angles along the x' and y' axes respectively, and $\mathbf{F} = -\kappa gh \cos(\theta) \tan(\phi) \mathbf{u} / \|\mathbf{u}\|$ where ϕ is the friction angle. Curvature terms representing the effects of coordinate transformations (Savage and Hutter 1991) are considered as second-order terms in this paper. A sketch of the situation is visible on Fig. 12.

These equations are solved by the code Avalanche, that simulates both landslides and generated tsunamis. While it has been used mainly with sources fully contained under water, e.g., Papua New Guinea (Heinrich et al. 2001a) and the 1979 landslide at

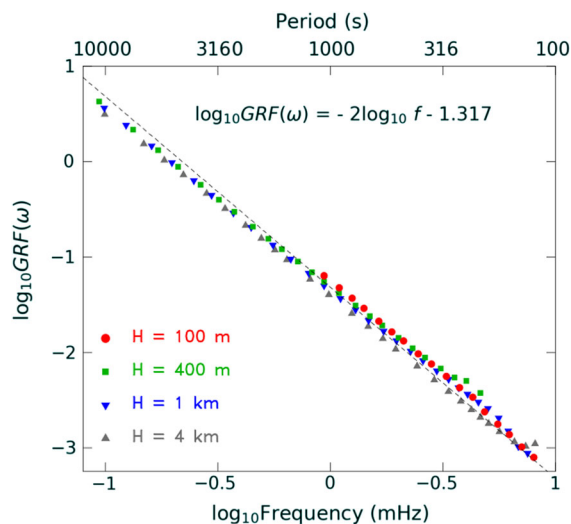


Figure 10

“Gilbert Response Function” $GRF(\omega)$ defined by Okal (2007), computed theoretically as a function of frequency for oceanic models of various depths. This figure is a generalization of Figure 10 of Okal (2007), and uses a logarithmic scale for frequency, to emphasize the power law behavior of $GRF(\omega)$; note that it is essentially independent of the water depth H . The dashed line is the regression (3) used in the deconvolution

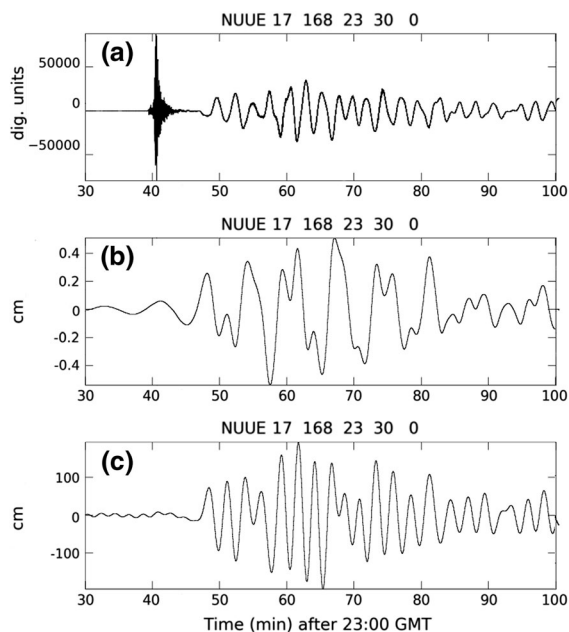


Figure 11

Deconvolution of the sea-surface tsunami amplitude $\eta(t)$ from the seismic record at NUUG. **a** Raw S11°E seismogram (see Fig. 7). **b** Apparent horizontal motion recorded by the instrument, after deconvolution of the instrument response. **c** Reconstructed time series $\eta(t)$ after deconvolution of the Gilbert Response Function

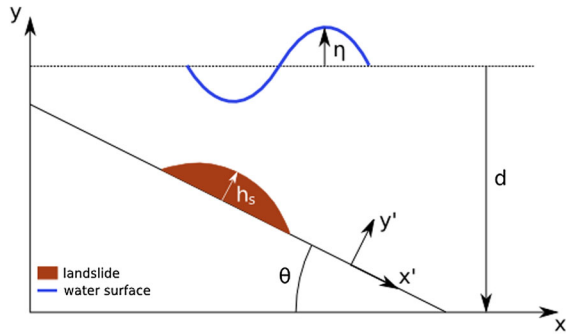


Figure 12

Sketch of our landslide-generated tsunami model. Along the x' and y' axes, h_s is the slide's thickness and along the x and y axes, η is the water surface elevation, d the unperturbed depth and θ the steepest slope angle

Mururoa (Poupardin et al. 2017), it was developed with the capacity to handle hybrid sources involving both subaerial debris flow and underwater sliding, as validated by the successful modeling of the 1997 Montserrat tsunami (Heinrich et al. 2001b) and the 2003 Montagne Pelée collapse event (Le Friant et al. 2003), this approach being similar to Weiss et al.'s (2009) simulation of the Lituya Bay event.

The shape of the bathymetry is typical of a fjord, with an abrupt slope (ranging from 40° to 60°) along the coasts. Due to this topography, ϕ is fixed at 50° . While this value may appear high, it results in a physically acceptable speed of the landslide: for a smaller friction angle of 30° we would obtain unrealistic aerial speeds of more than 200 m/s; with $\phi = 50^\circ$, we obtain a maximum aerial speed of 85 m/s, which is still very high: while a maximum speed of 100 m/s has been suggested for aerial landslides (e.g., Satake et al. 2002), this figure was proposed based on the value of 70 m/s, documented by filming the avalanche during the 1980 eruption of Mount Saint Helens (Voight 1981), which involved a powerful atmospheric explosion as the triggering mechanism. In the present case, we obtain a runout length of ~ 5000 m and a vertical fall height of ~ 1900 m.

4.2. Tsunami Model

Our strategy for the tsunami propagation is to start with the Saint–Venant equations during 80 s to

simulate the tsunami generation in shallow water, then to continue with the Boussinesq model in order to take into account any possible dispersive effects. We use the code *Avalanche* to solve the Saint–Venant equations, which are Navier–Stokes equations integrated over depth:

$$\frac{\partial \eta}{\partial t} + \frac{\partial(hu)}{\partial x} + \frac{\partial(hv)}{\partial y} = -\frac{\partial d}{\partial t}; \quad (7)$$

$$\frac{\partial u}{\partial t} + u \frac{\partial u}{\partial x} + v \frac{\partial u}{\partial y} = -g \frac{\partial \eta}{\partial x} + F_x; \quad (8)$$

$$\frac{\partial v}{\partial t} + u \frac{\partial v}{\partial x} + v \frac{\partial v}{\partial y} = -g \frac{\partial \eta}{\partial y} + F_y \quad (9)$$

where η is the surface elevation, $h = \eta + d$ the water column height where d is the unperturbed depth, u and v the depth-averaged velocities along the x and y axes and F_x and F_y the friction and Coriolis forces along the x and y axes, which remain negligible on the scale of the present experiment.

The sea-bottom deformation $\partial d / \partial t$ in Eq. (7) is computed as a forcing term:

$$\frac{\partial d}{\partial t} = \frac{1}{\cos \theta} \frac{\partial h_s}{\partial t} \quad (10)$$

Avalanche can also use a Boussinesq model, following Løvholdt et al. (2008):

$$\frac{\partial \eta}{\partial t} + \frac{\partial(hu)}{\partial x} + \frac{\partial(hv)}{\partial y} = -\frac{\partial d}{\partial t}; \quad (11)$$

$$\begin{aligned} \frac{\partial u}{\partial t} + u \frac{\partial u}{\partial x} + v \frac{\partial u}{\partial y} = & -g \frac{\partial \eta}{\partial x} + \frac{d^3}{3} \left[\frac{\partial^2 u_t}{\partial x^2} + \frac{\partial^2 v_t}{\partial x \partial y} \right] \\ & + \frac{d}{2} \left[u_t \frac{\partial^2 d}{\partial x^2} + u_t \frac{\partial^2 d}{\partial x \partial y} \right] + d \frac{\partial d}{\partial x} \frac{\partial u_t}{\partial x} \\ & + \frac{d}{2} \left[\frac{\partial d}{\partial x} \frac{\partial v_t}{\partial y} + \frac{\partial d}{\partial y} \frac{\partial v_t}{\partial x} \right] + F_x; \end{aligned} \quad (12)$$

$$\begin{aligned} \frac{\partial v}{\partial t} + u \frac{\partial v}{\partial x} + v \frac{\partial v}{\partial y} = & -g \frac{\partial \eta}{\partial y} + \frac{d^3}{3} \left[\frac{\partial^2 v_t}{\partial y^2} + \frac{\partial^2 u_t}{\partial x \partial y} \right] \\ & + \frac{d}{2} \left[v_t \frac{\partial^2 d}{\partial y^2} + v_t \frac{\partial^2 d}{\partial x \partial y} \right] + d \frac{\partial d}{\partial y} \frac{\partial v_t}{\partial y} \\ & + \frac{d}{2} \left[\frac{\partial d}{\partial x} \frac{\partial u_t}{\partial y} + \frac{\partial d}{\partial y} \frac{\partial u_t}{\partial x} \right] + F_y \end{aligned} \quad (13)$$

where u_t and v_t the time-derivatives of u and v .

Both the landslide and Saint–Venant equations, which are very similar, are solved by Godunov’s finite-volume scheme, extended to second order by a Van Leer scheme (Heinrich and Piatanesi 2000; Labbé et al. 2012).

The lone bathymetric dataset available in the region, the International Bathymetric Chart of the Arctic Ocean (IBCAO) (Jakobsson et al. 2012), only features a 500-m resolution; we had to interpolate it to a sampling of 25 m, in order to project the slide over more than a single pixel. After cropping, we obtain a bathymetric map of a 25×60 km² area, covering the slide’s location and the village of Nuugaatsiaq located 32 km SSW from the source.

However, we found that the maximum depth proposed in Karrat Fjord (430 m) is clearly too shallow, as it results in propagation times to Nuugaatsiaq of 14 min, incompatible with the difference in time of only 8 min documented on the seismic record at NUUG between the seismic and tsunami waves. For this reason, we later increased all depths in the fjord by an admittedly arbitrary factor of 2.

5. Results and Discussion

5.1. Results for the 2017 Event

The results are analyzed at a number of virtual gauges (Fig. 13) located in front of the landslide

(Gauge 1), then along the path of the tsunami (Gauges 2 and 3), and finally in front of the village of Nuugaatsiaq (Gauge 4).

Our first simulations, using the bathymetry of Model IBCAO (Jakobsson et al. 2012) with a maximum depth of 430 m in Karrat Fjord, predict a travel time of ~ 12 min to Nuugaatsiaq, about 4 min longer than observed on the seismic recording at NUUG (Fig. 14). We first note that the misfit in travel is much longer than the initial duration of the wave at Gauge 1 (Fig. 15); thus it cannot be a source effect, and is clearly due to propagation, from Gauge 1 to Gauge 4. In addition, Chao et al. (2018) have similarly noticed that the tsunami is observed on the NUUG seismometers about 5 min earlier than simulated using GEBCO bathymetry. They explain this discrepancy by interpreting the seismic signal as generated by the impact of the tsunami on a coastline located about 15 km upstream Karrat Fjord. Based on our observation that onland seismic recordings of tsunami falter at distances of a fraction of wavelength (Okal 2007), and on the horizontal polarization of the recordings (Fig. 9), we prefer to invoke an inaccurate bathymetry in Karrat Fjord.

In this context, we decided to increase the water depth by a factor of two across the board, with a new maximum value of 860 m. Under the Saint–Venant approximation, this admittedly arbitrary correction increases the tsunami velocity (and reduces the travel

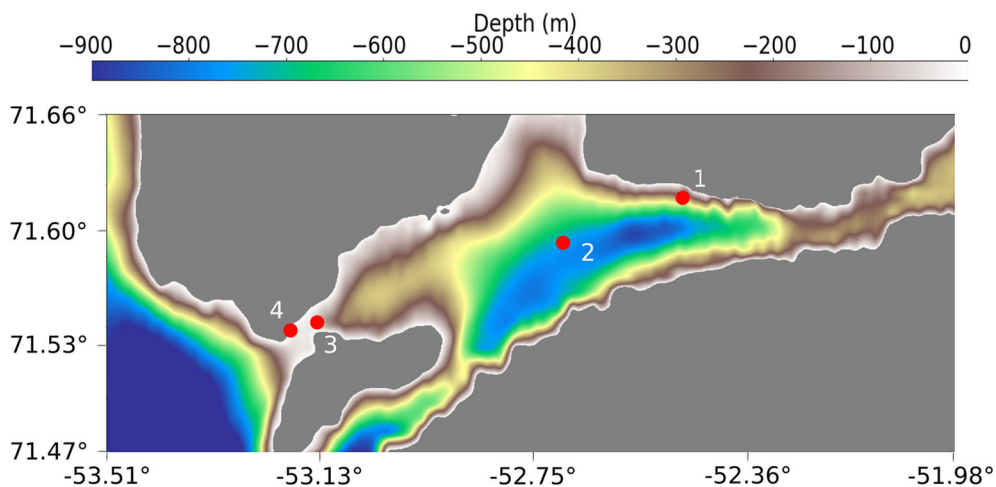


Figure 13

Bathymetric grid in Karrat Fjord and gauge locations (red dots) along the path of the tsunami. The tsunami is initialized at Gauge 1, and progresses to Gauges 2, 3 and finally 4 in front of Nuugaatsiaq

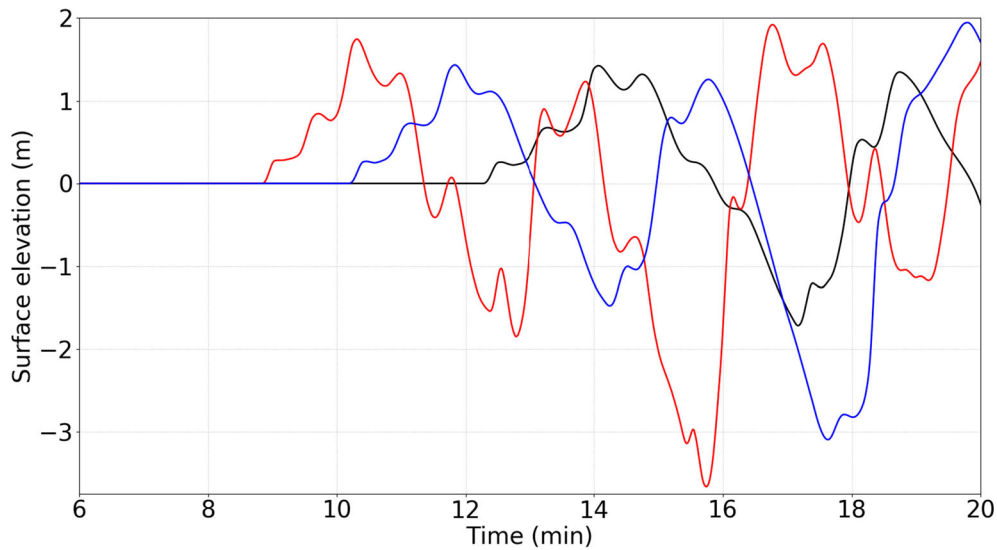


Figure 14

Surface elevation at Gauge 4 (in front of Nuugaatsiaq) for the initial bathymetry (black), increased by a factor 1.5 (blue) and by a factor 2 (red), simulated by the Saint–Venant model

time) by a factor of $\sqrt{2}$ (Fig. 14); in the Boussinesq model used herein, where the relationship between velocity and square root of depth is not linear, the effect is only slightly smaller, and in both models the leading wave now reaches the village in ~ 8 min, in much better agreement with the observed arrival time.

While our correction of the fjord bathymetry may appear drastic, we stress that a similar situation was documented recently in Palu Bay, Sulawesi; following the earthquake and tsunami of 28 September 2018, it became clear that the bathymetry available from global models such as IBCAO or GEBCO grossly underestimated (by a factor as large as 4) the

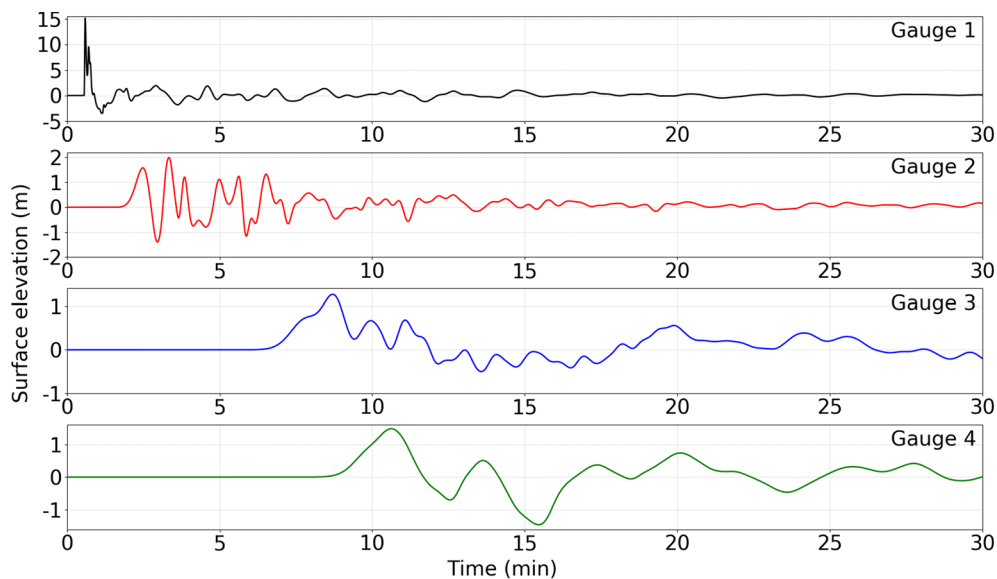


Figure 15

Surface elevations for Gauges 1, 2, 3 and 4, obtained with the Boussinesq model

water depth in the bay (Fritz et al. 2018b). We must conclude that such models cannot pretend to give a reliable small-scale bathymetry, especially in profoundly indented bays such as Karrat Fjord, where the proposed bathymetry is most likely inaccurate.

Under our model of deepened bathymetry, and as shown on Fig. 15, water waves reach 15.5 m at the source (Gauge 1), 2 m at the maximum depth (Gauge 2), 1.3 m before Nuugaatsiaq (Gauge 3) and 1.5 m in front of Nuugaatsiaq (Gauge 4). These figures are not directly comparable to the results of Fritz et al.'s (2018a) field survey, who reported run-up reaching 90 m in the source area, and 50 m on the opposite side of the 6-km wide fjord. We stress that our simulations do not include run-up computations, and that our virtual gauges are located in deep water (340 and 750 m, respectively for Gauges 1 and 2).

We obtain a wave-train at Gauge 4 (in front of Nuugaatsiaq) similar to the signal recorded at the seismic station (Fig. 16), featuring three waves with a period of ~ 3 min (see Gauge 4 on Fig. 15).

Finally, we note on Fig. 16 that while the amplitude of the simulated wave is on the same order (1.5 m) as that deconvolved in a comparable time window from the S11°E component of the NUUG seismometer (1.0 m), the simulated wave features significantly lower frequencies (4.6–5.4 mHz vs. 6.2 mHz), presumably as a result of seiche in the channel, which may also explain the longer duration (and later higher amplitudes) of the deconvolved time series. Nevertheless, the acceptable agreement between them serves as an *a posteriori* validation of the deconvolution procedure in Sect. 3.3.

Although we used the Boussinesq model to simulate the tsunami, results show (Fig. 17) that three water waves are still observed within the first 12 min when using the Saint-Venant equations. This suggests that the generation of these three water waves depends on the bathymetry's shape and is not a result of dispersive effects, but more probably of reflection on the coasts.

This is further confirmed through the use of Glimsdal et al.'s (2013) dimensionless parameter $\tau = 6ht/gT^3$, where h is water depth, t travel time and T dominant period. In the present case, the packet of three waves corresponds to $\tau \approx 0.03$, which is clearly

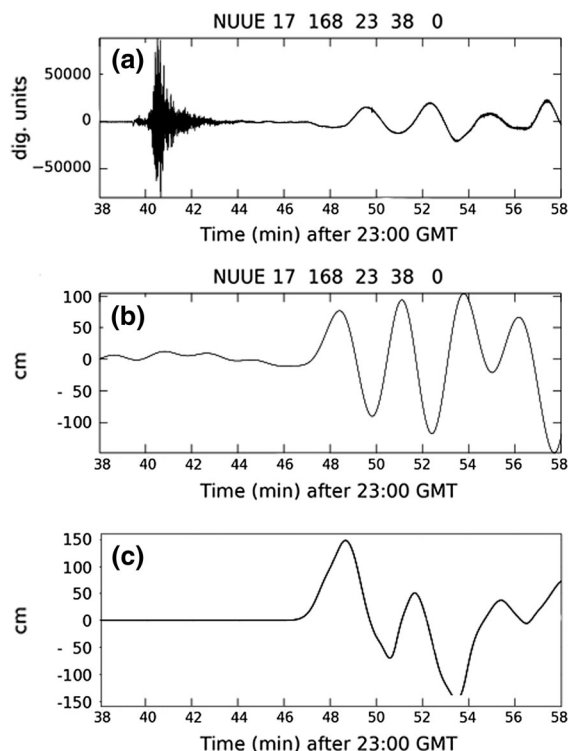


Figure 16

Comparison of recorded and simulated tsunami waveshapes. **a, b** Respectively the raw seismogram and the deconvolved tsunami amplitude η for a time window starting at 23:38 GMT (72 s before the initiation of the slide), and lasting 20 min; they are close-ups of Frames (a, c) of Fig. 11. **c** Simulated tsunami wave at Gauge 4 (in front of Nuugaatsiaq); this is simply a 20-min window of frame **b** of Fig. 15. Note the good agreement of amplitudes between (b) and (c), but the lower-frequency character of the simulated wave

below the value of 0.5 given by the authors as a threshold for significant dispersion effects (following Shuto 1991).

On Fig. 20, maximum elevations through the entire simulation show that the water level reaches up to 40 m at the source, and we then observe a decrease of the water heights due to propagation in deeper water. Finally the water waves reach between 1 and 1.5 m at Nuugaatsiaq.

While we eventually obtained a good agreement between our simulations and the seismic recording at NUUG, we note that we had to significantly increase (by a factor of 2) the field of depths available from published bathymetric charts, confirming if need be, the critical role of an accurate bathymetry in allowing realistic simulations of the propagation of tsunamis in

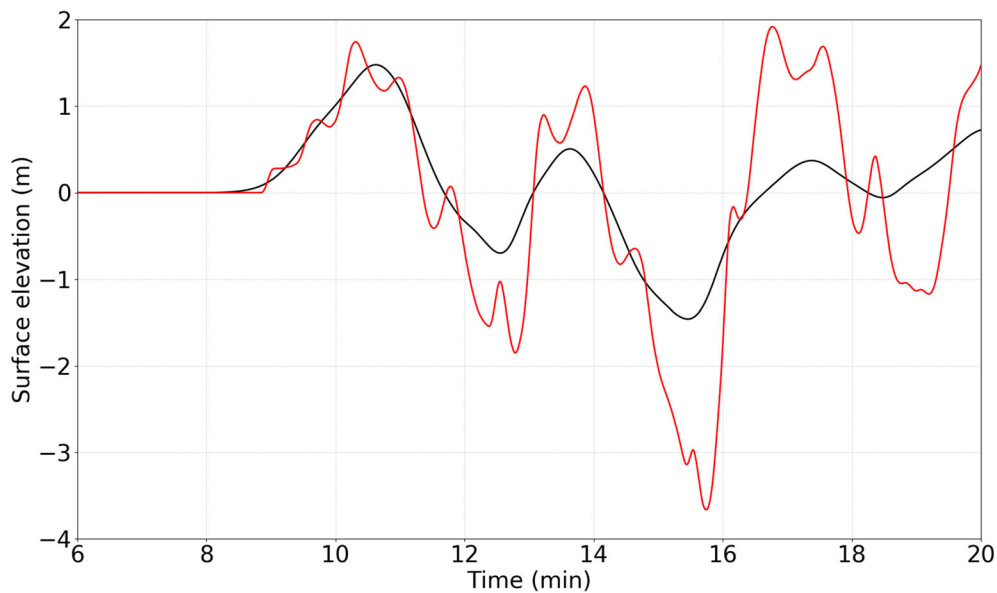


Figure 17

Surface elevation at Gauge 4 simulated by the Boussinesq model (black curve) and the Saint-Venant model (red curve)

complex, poorly chartered marine environments. For the sake of simplicity, we used an across-the-board, constant, and indeed arbitrary, factor of 2 which

provided an adequate gain of about 4 min in travel-time. In particular, we did not try more sophisticated, laterally variable, corrections to the available

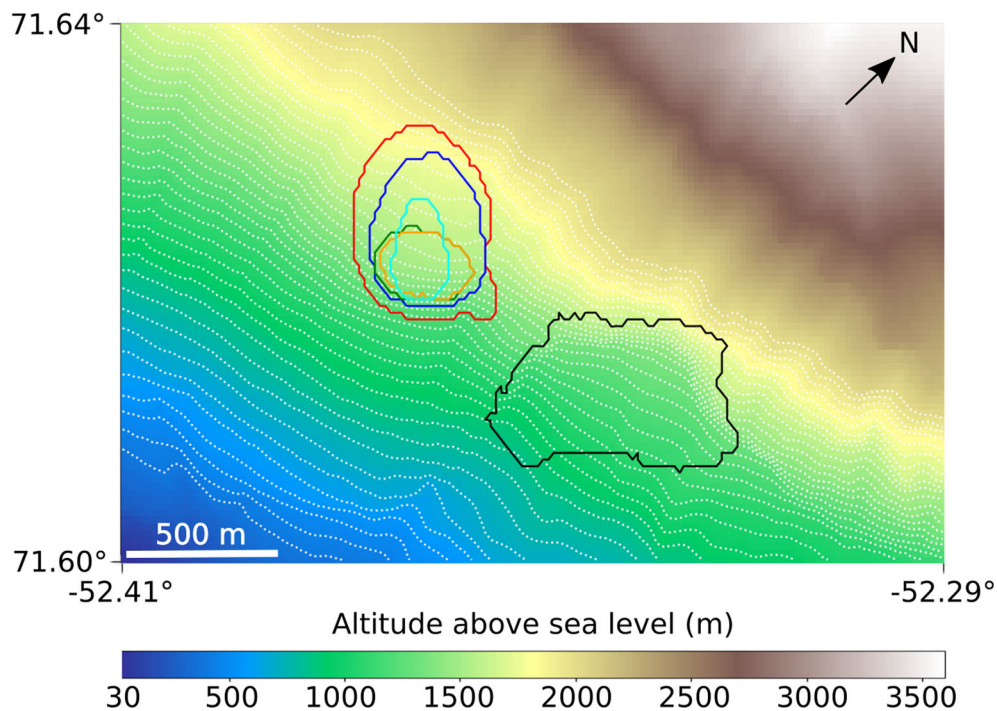


Figure 18

Footprints of the various landslides, the 2017 event (black) and the western hypothetical volumes of 38 million m³ (red), 14 million m³ (blue), 7 million m³ (green), 2 million m³ “E–W” (orange) and 2 million m³ “N–S” (cyan)

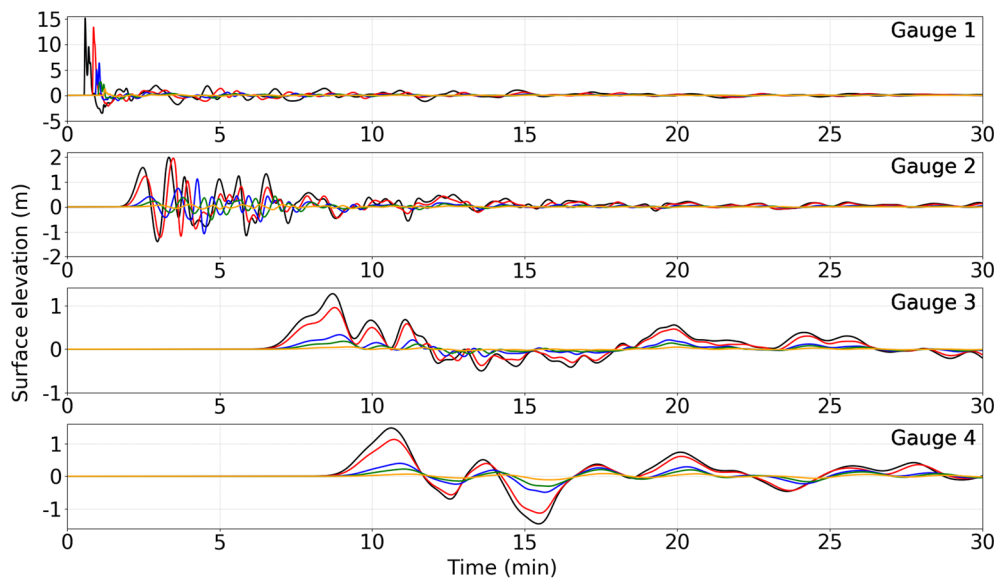


Figure 19

Surface elevations for different volumes of landslide on Gauges 1, 2, 3 and 4, for the 2017 event of 53 million m^3 (black) and for the potential events of 38 million m^3 (red), 14 million m^3 (blue), 7 million m^3 (green) and 2 million m^3 (orange)

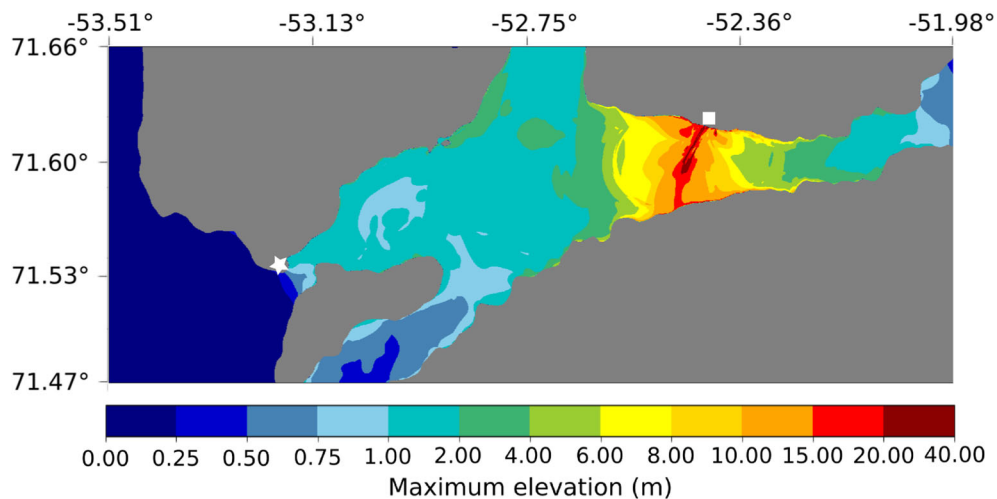


Figure 20

Maximal surface elevations simulated between the source (white square) and the village of Nuugaatsiaq (white star) for the 2017 event of 53 million m^3

bathymetry, which would have been futile, given its present quality, which the original misfit of travel times documents as grossly erroneous. In view of the potential for failure of the Western slide, and in the context of the general regional hazard expressed by the previous tsunamis of 1952, 2000, and to a lesser extent, 1954 and 2012 (see Sect. 2 for details), a high-quality bathymetric survey would be desirable

in Karrat Fjord, and in the other fjords with populated settlements on their shores.

5.2. The Next, Potential, Event: Sensitivity Studies on Its Volume and Shape

We now address the question of the “next” slide, *i.e.*, the potential failure of the material immediately

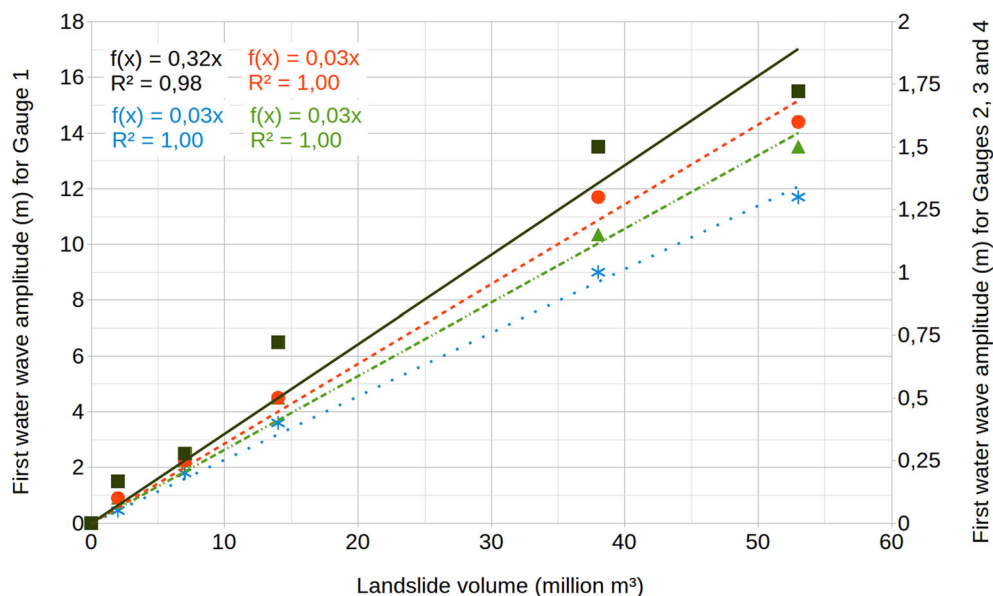


Figure 22

Amplitude (in m) of the first generated water wave vs. the landslide volume (in million m^3), for Gauges 1 (black squares, solid line, left vertical scale), 2 (red circles, dashed line, right vertical scale), 3 (blue asterisks, dotted line, right vertical scale) and 4 (green triangles, dash-dotted line, right vertical scale). Gauges 2, 3 and 4 are referred to the right scale while Gauge 1 is referred to the left scale

to the West of the 2017 slide (Fig. 2). Unlike for the latter, we can only speculate as to its volume, shape and of course timing. In order to investigate the impact of that potential event, and in particular, the influence of its volume, we consider four landslide geometries of variable volume, ranging from 2 million m^3 (hereafter Model “E–W”) to 7, 14 and 38 million m^3 , respectively (Fig. 18; Table 1), and also compare our results with those of the 2017 slide (53 million m^3).

The range of volumes proposed here (2–38 million m^3) remains small, as compared to that studied by Scheidegger (1973), and thus the range of friction angles derived from the application of his power law (with an exponent of $-1/6$) between volume and friction coefficient, is only a few degrees (from 15 to 23). A similar range of friction angles was studied in Mergili et al. (2017), showing some difference in runout between 15° and 23° , for a rock avalanche of 6.4 million m^3 . Nevertheless, we have argued in Sect. 4.1 that such angles would lead to unrealistic velocities upon reaching the water. In this context, we keep a friction angle of 50° for the present calculations. The landslide rheology is a major source of uncertainties when considering the

landslide dynamics. However, its effect is of the second order when considering the water waves amplitudes.

Simulated time series are compiled on Fig. 19; note that for the various scenarios of the Western slide, Gauge 1 is moved 1 km to the West, without significant difference in water depth (Fig. 20). In addition, Fig. 21 maps maximum wave elevations for the various western slides.

Figure 19 documents a good linearity between the volume of the landslides and the simulated water heights, as evidenced directly in front of the slide (Gauge 1), as well as farther along the path of the tsunami (Gauges 2, 3, and 4). For example, the largest case simulated (38 million m^3) from the

Table 1

Summary of dimensions and volumes of the western landslide

Volume (million m^3)	Width \times length \times thickness (m, max)	Altitude (m, center)
38	400 \times 600 \times 200	1500
14	300 \times 500 \times 146	1550
7	250 \times 200 \times 171	1500
2 “E–W”	250 \times 200 \times 110	1500
2 “N–S”	125 \times 400 \times 103	1500

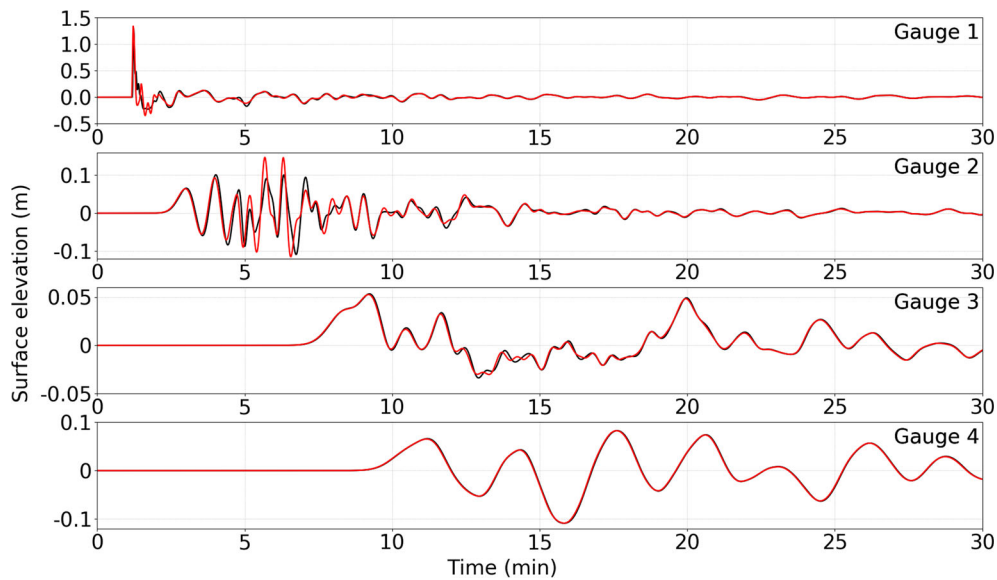


Figure 23
Surface elevations comparison for the 2 million m³ “E–W” (black) and “N–S” (red), at Gauges 1, 2, 3 and 4

western landslide is smaller than the 2017 slide by a factor of 1.5, and the resulting water waves by a comparable factor (1.3). At the next lower level (14 million m³), the water height remains 40 cm, which still presents a risk for the population. Dividing this volume by two, we obtain a water height of 20 cm, which is considered the limit of hazard for flooding by a tsunami. This linear relationship between the first generated water wave amplitude and the landslide volume is confirmed on Fig. 22 by excellent regression coefficients [$R^2 = 0.99$ for Gauge 1, black: $R^2 = 1.00$ with two significant digits for Gauges 2, 3, 4 (red, blue, green)]. We note that the least linear relationship is for Gauge 1, located in the area where we use the Saint–Venant equations, so it appears that the linearity is most valid for the Boussinesq model.

Finally, we explore the possible influence of the shape of the landslide on the characteristics of the tsunami, such as its amplitude and dominant period. For this purpose, we consider a landslide (Model “N–S”) with the same volume (2 million m³) as our smallest “E–W” scenario (*d*), but with a narrower and taller footprint (shown in cyan on Fig. 18, and detailed in Table 1). Figure 23 presents the surface elevation comparison at the different gauges for the “E–W” and “N–S” 2 million m³ western landslides and shows no significant difference either in

amplitude or dominant period between the two cases, allowing us to conclude that the total volume of the slide is the primary factor controlling the characteristics of the wave.

6. Conclusion

Simulation of the tsunami generated by the landslide of June 17, 2017 in Karrat Fjord, Greenland satisfactorily matches both inferred wave activity at Nuugaatsiaq, 32 km WSW of the source, and the early portion of the signal recorded at the seismic station NUUG. Using a slide volume of ~ 50 million m³, we model three water waves with periods of ~ 3 min, reaching the village of Nuugaatsiaq after 8 min. While these results are satisfying, they require doubling the depths documented by available bathymetry; this effect cannot be simply an artifact of our forced interpolation (from a 500 to a 25-m resolution) of the IBCAO dataset, and thus attests to the poor quality of the latter.

Our sensitivity study on different scenarios for the potential landslide, immediately to the West of the 2017 scar, supports a general linearity between their volumes and the heights of resulting tsunami waves. Using a threshold of 30 cm (at Gauge 4, considered as

a “last”, initially wet grid point) for a potentially hazardous tsunami at Nuugaatsiaq, we estimate that it corresponds to a 7 million m³ slide, considerably smaller than the more realistic volume of 38 million m³ regarded as precarious to the West of the 2017 event, a scenario which would lead to a level flooding and destruction comparable to the 2017 event.

Acknowledgements

We thank John Clinton, Director of Seismic Networks, ETH, Zürich, for access to the NUUG seismograms, and for critical metadata concerning their misorientation. Some figures were produced using the GMT software (Wessel and Smith 1991). This work was supported by the LRC Yves Rocard (Laboratoire de Recherche Conventionné CEA-ENS). The paper was improved by the constructive comments of David Tappin and a second, anonymous, reviewer.

Publisher's Note Springer Nature remains neutral with regard to jurisdictional claims in published maps and institutional affiliations.

REFERENCES

- Abadie, S. M., Harris, J. C., Grilli, S. T., & Fabre, R. (2012). Numerical modeling of tsunami waves generated by the flank collapse of the Cumbre Vieja Volcano (La Palma, Canary Islands): Tsunami source and near field effects. *Journal of Geophysical Research Oceans*, 117(5), 1–26.
- Ambraseys, N., & Bilham, R. (2012). The Sarez–Pamir earthquake and landslide of 18 February 1911. *Seismological Research Letters*, 83(2), 294–314.
- Assier-Rzadkiewicz, S., Heinrich, P., Sabatier, P. C., Savoye, B., & Bourillet, J. F. (2000). Numerical modelling of a landslide-generated Tsunami: The 1979 nice event. *Pure and Applied Geophysics*, 157(10), 1707–1727.
- Chao, W.-A., Wu, T.-R., Ma, K.-F., Kuo, Y.-T., Wu, Y.-M., Zhao, L., et al. (2018). The large greenland landslide of 2017: Was a Tsunami warning possible? *Seismological Research Letters*, 89(4), 1335–1344.
- Clinton, J., Larsen, T., Dahl-Jensen, T., Voss, P., & Nettles, M. (2017). Special event: Nuugaatsiaq Greenland landslide and tsunami. *Incorporated Research Institutions for Seismology Washington DC*. <https://ds.iris.edu/ds/nodes/dmc/specialevents/2017/06/22/nuugaatsiaq-greenland-landslide-and-tsunami/>.
- Dahl-Jensen, T., Larsen, L. M., Pedersen, S. A. S., Pedersen, J., Jepsen, H. F., Pedersen, G., et al. (2004). Landslide and Tsunami 21 November 2000 in Paatuut, West Greenland. *Natural Hazards*, 31(1), 277–287.
- Ekström, G., & Stark, C. P. (2013). Simple scaling of catastrophic landslide dynamics. *Science*, 339(6126), 1416–1419.
- Fine, I. V., Rabinovich, A. B., Thomson, R. E., & Kulikov, E. A. (2003). *Numerical modeling of Tsunami generation by submarine and subaerial landslides* (pp. 69–88). Dordrecht: Springer.
- Fritz, H. M. (2002). *Initial phase of landslide generated impulse waves*. PhD Thesis, ETH Zurich.
- Fritz, H. M., Giachetti, T., Anderson, S., & Gauthier, D. (2018a). Field survey of the 17 June 2017 landslide generated Tsunami in Karrat Fjord, Greenland. In *EGU General Assembly Conference Abstracts*, Vol. 20 of *EGU General Assembly Conference Abstracts*, p. 18345.
- Fritz, H. M., Synolakis, C., Kalligeris, N., Skanavis, V., Santoso, F., Rizal, M., et al. (2018b). Field survey of the 28 September 2018 Sulawesi tsunami. *Eos Transactions American Geophysical Union*, 99, 53. (NH22B-04, [abstract]).
- Gauthier, D., Anderson, S. A., Fritz, H. M., & Giachetti, T. (2018). Karrat Fjord (Greenland) tsunamigenic landslide of 17 June 2017: Initial 3D observations. *Landslides*, 15(2), 327–332.
- Geist, E. L. (2000). Origin of the 17 July 1998 Papua New Guinea Tsunami: Earthquake or landslide. *Seismological Research Letters*, 71(3), 344–351.
- Gilbert, J. (1980). An introduction to low-frequency seismology. In A. Dziewopinski & E. Boschi (Eds.), *Proceedings of the International School of Physics “Enrico Fermi”* (Vol. 78, pp. 41–81). Amsterdam: North Holland.
- Glimsdal, S., Pedersen, G. K., Harbitz, C. B., & Løvholt, F. (2013). Dispersion of tsunamis: Does it really matter? *Natural Hazards and Earth System Sciences*, 13, 1507–1526.
- Guérin, C. (2017). Effect of the DTM quality on the bundle block adjustment and orthorectification process without GCP: Example on a steep area. In *Proceedings of 2017 IEEE international geoscience remote sensing symposium (IGARSS)*. IEEE, pp. 1067–1070.
- Guérin, C., Binet, R., & Pierrot-Deseilligny, M. (2014). Automatic detection of elevation changes by differential DSM analysis: Application to urban areas. *IEEE Journal of Selected Topics in Applied Earth Observations and Remote Sensing*, 7(10), 4020–4037.
- Haerberli, W., & Gruber, S. (2009). *Global warming and mountain permafrost* (pp. 205–218). Berlin: Springer.
- Hanson, J. A., & Bowman, J. R. (2005). Dispersive and reflected tsunami signals from the 2004 Indian Ocean tsunami observed on hydrophones and seismic stations. *Geophysical Research Letters*, 32, 17.
- Hébert, H., Piatanesi, A., Heinrich, P., & Schindelé, F. (2002). Numerical modeling of the September 13, 1999 landslide and tsunami on Fatu Hiva Island (French Polynesia). *Geophysical Research Letters*, 29(10), 10–13.
- Heinrich, P., Boudon, G., Komorowski, J. C., Sparks, R. S. J., Herd, R., & Voight, B. (2001b). Numerical simulation of the December 1997 Debris Avalanche in Montserrat, Lesser Antilles. *Geophysical Research Letters*, 28(13), 2529–2532.
- Heinrich, P., & Piatanesi, A. (2000). Near-field modeling of the July 17, 1998 tsunami in Papua New Guinea. *Geophysical Research Letters*, 27(19), 3037–3040.
- Heinrich, P., Piatanesi, A., & Hébert, H. (2001a). Numerical modelling of tsunami generation and propagation from

- submarine slumps: The 1998 Papua New Guinea event. *Geophysical Journal International*, 145(1), 97–111.
- Hermanns, R. L., Blikra, L. H., Naumann, M., Nilsen, B., Panthi, K. K., Stromeyer, D., et al. (2006). Examples of multiple rock-slope collapses from Köfels (Ötztal valley, Austria) and western Norway. *Engineering Geology*, 83(1–3), 94–108.
- Higman, B., Shugar, D. H., Stark, C. P., Ekström, G., Koppes, M. N., Lynett, P., et al. (2018). The 2015 landslide and tsunami in Taan Fiord, Alaska. *Scientific Reports*, 8(1), 12993.
- Huggel, C., Clague, J. J., & Korup, O. (2012). Is climate change responsible for changing landslide activity in high mountains? *Earth Surface Processes and Landforms*, 37(1), 77–91.
- ICAO. (1955). International Civil Aviation (ICAO) Meteorological Stations in Greenland. *ICAO Bulletin*, 10(7), 7–11.
- Jakobsson, M., Mayer, L., Coakley, B., Dowdeswell, J. A., Forbes, S., Fridman, B., et al. (2012). The international bathymetric chart of the Arctic Ocean (IBCAO) Version 3.0. *Geophysical Research Letters*, 39, L12609.
- La Rocca, M., Galluzzo, D., Saccorotti, G., Tinti, S., Cimini, G. B., & Del Pezzo, E. (2004). Seismic signals associated with landslides and with a tsunami at Stromboli volcano, Italy. *Bulletin of the Seismological Society of America*, 94(5), 1850–1867.
- Labbé, M., Donnadieu, C., Daubord, C., & Hébert, H. (2012). Refined numerical modeling of the 1979 tsunami in Nice (French Riviera): Comparison with coastal data. *Journal of Geophysical Research Earth Surface*, 117, F1.
- Le Friant, A., Heinrich, P., Deplus, C., & Boudon, G. (2003). Numerical simulation of the last flank-collapse event of Montagne Pelée, Martinique, Lesser Antilles. *Geophysical Research Letters*, 30, 2.
- Løvholt, F., Pedersen, G., & Gisler, G. (2008). Oceanic propagation of a potential tsunami from the La Palma Island. *Journal of Geophysical Research Oceans*, 113(9), 1–21.
- McNamara, D., Ringler, A., Hutt, C., & Gee, L. (2011). Seismically observed seiche in the Panama Canal. *Journal of Geophysical Research Solid Earth*, 116, B4.
- Mergili, M., Fischer, J.-T., Krenn, J., & Pudasaini, S. P. (2017). r.avaflow v1, and advances open-source computational framework for the propagation and interaction of two-phase mass flows. *Geoscientific Model Development*, 10(2), 553–569.
- Miller, D. J. (1960). Giant waves in Lituya Bay, Alaska. *US Geological Survey Professional Paper*, 354-C.
- Naranjo, J. A., Arenas, M., Clavero, J., & Muñoz, O. (2009). Mass movement-induced tsunamis: Main effects during the Patagonian Fjordland seismic crisis in Aisén (45° 25'S), Chile. *Andean Geology*, 36, 1.
- NOAA. (2018). *National Geophysical Data Center/ World Data Service: NCEI/WDS Global Historical Tsunami Database*. NOAA National Centers for Environmental Information. <https://data.nodc.noaa.gov/cgi-bin/iso?id=gov.noaa.ngdc.mgg.hazards:G02151>
- Okal, E. A. (2003). *T waves from the 1998 Papua New Guinea earthquake and its aftershocks: Timing the tsunamigenic slump*. *Pure and Applied Geophysics*, 160, 1843–1863.
- Okal, E. A. (2007). Seismic records of the 2004 Sumatra and other tsunamis: A quantitative study. *Pure and Applied Geophysics*, 164, 325–353.
- Okal, E. A., Fryer, G. J., Borrero, J. C., & Ruscher, C. (2002). The landslide and local tsunami of 13 September 1999 on Fatu Hiva (Marquesas islands; French Polynesia). *Bulletin de la Société géologique de France*, 173(4), 359–367.
- Okal, E. A., & Synolakis, C. E. (2001). Comment on “Origin of the 17 July 1998 Papua New Guinea tsunami: Earthquake or landslide?” by EL Geist. *Seismological Research Letters*, 72(3), 363–366.
- Okal, E. A., & Synolakis, C. E. (2003). A theoretical comparison of tsunamis from dislocations and landslides. *Pure and Applied Geophysics*, 160(10–11), 2177–2188.
- Pedersen, S. A. S., Larsen, L. M., Dahl-jensen, T., Jepsen, H. F., Krarup, G., Nielsen, T., et al. (2002). Tsunami-generating rock fall and landslide on the south coast of Nuussuaq, central West Greenland. *Geology of Greenland Survey Bulletin*, 191, 73–83.
- Pierrot-Deseilligny, M., Paparoditis, N. (2006). A multiresolution and optimization-based image matching approach: An application to surface reconstruction from SPOT5-HRS stereo imagery. In *IAPRS vol XXXVI-I/W41 in ISPRS Workshop On Topographic Mapping From Space (With Special Emphasis on Small Satellites, Ankara, Turquie)*.
- Pouliquen, O. (1999). Scaling laws in granular flows down rough inclined planes. *Physics of Fluids*, 11(3), 542–548.
- Poupardin, A., Heinrich, P., Frère, A., Imbert, D., Hébert, H., & Flouzat, M. (2017). The 1979 submarine landslide-generated Tsunami in Mururoa, French Polynesia. *Pure and Applied Geophysics*, 174, 3293–3311.
- Rodriguez, M., Chamot-Rooke, N., Hébert, H., Fournier, M., & Huchon, P. (2013). Owen Ridge deep-water submarine landslides: Implications for tsunami hazard along the Oman coast. *Natural Hazards and Earth System Science*, 13, 417–424.
- Saito, M. (1967). Excitation of free oscillations and surface waves by a point source in a vertically heterogeneous earth. *Journal of Geophysical Research*, 72(14), 3689–3699.
- Satake, K., Smith, J., & Shinozaki, K. (2002). *Three-dimensional reconstruction and tsunami model of the Nuanu and Wailau giant landslides* (pp. 333–346). American Geophysical Union Geophysical Monograph Series: Hawaii.
- Savage, S. B., & Hutter, K. (1989). The motion of a finite mass of granular material down a rough incline. *Journal of Fluid Mechanics*, 199, 177–215.
- Savage, S. B., & Hutter, K. (1991). The dynamics of avalanches of granular materials from initiation to runout. Part I: Analysis. *Acta Mechanica*, 86(1), 201–223.
- Scharroo, R., Smith, W., Titov, V., & Arcas, D. (2005). Observing the Indian Ocean tsunami with satellite altimetry. *Geophysical Research Abstracts*, 7, 230.
- Scheidegger, A. E. (1973). On the prediction of the reach and velocity of catastrophic landslides. *Rock Mechanics and Rock Engineering*, 5(4), 231–236.
- Schuster, R. L., & Alford, D. (2004). Usui landslide dam and lake sarez, Pamir mountains, Tajikistan. *Environmental and Engineering Geoscience*, 10(2), 151–168.
- Sepúlveda, S. A., & Serey, A. (2009). Tsunamigenic, earthquake-triggered rock slope failures during the April 21, 2007 Aisén earthquake, southern Chile (45.5 S). *Andean Geology*, 36, 1.
- Shuto, N. (1991). Numerical simulation of tsunamis—its present and near future. *Natural Hazards*, 4, 171–191.
- Synolakis, C. E., Bardet, J.-P., Borrero, J. C., Davies, H. L., Okal, E. A., Silver, E. A., Sweet, S., & Tappin, D. R. (2002). The slump origin of the 1998 Papua New Guinea tsunami. In *Proceedings of the Royal Society of London, Series A: Mathematical, Physical and Engineering Sciences*, Vol. 458, The Royal Society, pp. 763–789.

- Thomson, R. E., Rabinovich, A. B., Kulikov, E. A., Fine, I. V., & Bornhold, B. D. (2001). *On Numerical simulation of the landslide-generated Tsunami of November 3, 1994 in Skagway Harbor* (pp. 243–282). Dordrecht: Springer.
- Tinti, S., Pagnoni, G., & Zaniboni, F. (2006). The landslides and tsunamis of the 30th of December 2002 in Stromboli analysed through numerical simulations. *Bulletin of Volcanology*, 68(5), 462–479.
- Viroulet, S., Cébron, D., Kimmoun, O., & Kharif, C. (2013). Shallow water waves generated by subaerial solid landslides. *Geophysical Journal International*, 193(2), 747–762.
- Voight, B. (1981). The 1980 eruptions of Mount St. Helens, Washington. Time scale for the first moments of the May 18 eruption. *US Geological Survey Professional Paper*, 1250, 69–86.
- Wang, J., Ward, S. N., & Xiao, L. (2015). Numerical simulation of the December 4, 2007 landslide-generated tsunami in Chehalis Lake, Canada. *Geophysical Journal International*, 201(1), 372–376.
- Ward, S. N. (1980). Relationships of tsunami generation and an earthquake source. *Journal of Physics of the Earth*, 28(5), 441–474.
- Ward, S. N., & Day, S. (2011). The 1963 landslide and flood at Vajont Reservoir Italy. A tsunami ball simulation. *Italian Journal of Geosciences*, 130(1), 16–26.
- Weiss, R., Fritz, H. M., & Wünnemann, K. (2009). Hybrid modeling of the mega-tsunami runup in Lituya Bay after half a century. *Geophysical Research Letters*, 36, 9.
- Wessel, P., & Smith, W. H. F. (1991). Free software helps map and display data. *Eos Transactions American Geophysical Union*, 72(41), 441–446.
- Yuan, X., Kind, R., & Pedersen, H. A. (2005). Seismic monitoring of the Indian Ocean tsunami. *Geophysical Research Letters*, 32, 15.

(Received September 13, 2018, revised January 29, 2019, accepted January 31, 2019, Published online February 11, 2019)

Terms and Conditions

Springer Nature journal content, brought to you courtesy of Springer Nature Customer Service Center GmbH (“Springer Nature”). Springer Nature supports a reasonable amount of sharing of research papers by authors, subscribers and authorised users (“Users”), for small-scale personal, non-commercial use provided that all copyright, trade and service marks and other proprietary notices are maintained. By accessing, sharing, receiving or otherwise using the Springer Nature journal content you agree to these terms of use (“Terms”). For these purposes, Springer Nature considers academic use (by researchers and students) to be non-commercial.

These Terms are supplementary and will apply in addition to any applicable website terms and conditions, a relevant site licence or a personal subscription. These Terms will prevail over any conflict or ambiguity with regards to the relevant terms, a site licence or a personal subscription (to the extent of the conflict or ambiguity only). For Creative Commons-licensed articles, the terms of the Creative Commons license used will apply.

We collect and use personal data to provide access to the Springer Nature journal content. We may also use these personal data internally within ResearchGate and Springer Nature and as agreed share it, in an anonymised way, for purposes of tracking, analysis and reporting. We will not otherwise disclose your personal data outside the ResearchGate or the Springer Nature group of companies unless we have your permission as detailed in the Privacy Policy.

While Users may use the Springer Nature journal content for small scale, personal non-commercial use, it is important to note that Users may not:

1. use such content for the purpose of providing other users with access on a regular or large scale basis or as a means to circumvent access control;
2. use such content where to do so would be considered a criminal or statutory offence in any jurisdiction, or gives rise to civil liability, or is otherwise unlawful;
3. falsely or misleadingly imply or suggest endorsement, approval, sponsorship, or association unless explicitly agreed to by Springer Nature in writing;
4. use bots or other automated methods to access the content or redirect messages
5. override any security feature or exclusionary protocol; or
6. share the content in order to create substitute for Springer Nature products or services or a systematic database of Springer Nature journal content.

In line with the restriction against commercial use, Springer Nature does not permit the creation of a product or service that creates revenue, royalties, rent or income from our content or its inclusion as part of a paid for service or for other commercial gain. Springer Nature journal content cannot be used for inter-library loans and librarians may not upload Springer Nature journal content on a large scale into their, or any other, institutional repository.

These terms of use are reviewed regularly and may be amended at any time. Springer Nature is not obligated to publish any information or content on this website and may remove it or features or functionality at our sole discretion, at any time with or without notice. Springer Nature may revoke this licence to you at any time and remove access to any copies of the Springer Nature journal content which have been saved.

To the fullest extent permitted by law, Springer Nature makes no warranties, representations or guarantees to Users, either express or implied with respect to the Springer nature journal content and all parties disclaim and waive any implied warranties or warranties imposed by law, including merchantability or fitness for any particular purpose.

Please note that these rights do not automatically extend to content, data or other material published by Springer Nature that may be licensed from third parties.

If you would like to use or distribute our Springer Nature journal content to a wider audience or on a regular basis or in any other manner not expressly permitted by these Terms, please contact Springer Nature at

onlineservice@springernature.com